Narrowband to Broadband Conversion with Spatially Autocorrelated Reflectance Measurements

ZHANQING LI AND H. G. LEIGHTON

Department of Meteorology, McGill University, Montreal, Quebec, Canada

(Manuscript received 9 April 1991, in final form 18 August 1991)

ABSTRACT

A new technique for estimating broadband reflectance from Advanced Very High-Resolution Radiometer (AVHRR) narrowband reflectances in channel 1 and 2 is developed. The data used are simultaneous and coincident narrowband and broadband measurements made by the AVHRR and Earth Radiation Budget Experiment (ERBE) radiometers aboard *NOAA-9* during four days in July 1985 in the region north of 60°N. The limitations and inefficiency of classical regressional methods when applied to datasets with high spatial autocorrelation, which is often the case for remotely sensed data, are discussed. A statistical variable, Moran's I, is introduced, which is specifically designed for testing against a null hypothesis of spatial independence. On the basis of Moran's I and a correlogram analysis of the spatial autocorrelation of measured reflectances, the data are sampled to provide a spatially independent dataset. In addition to sampling, the data are also screened with respect to spatial homogeneity. Both scene-dependent and scene-independent regressional models are developed that are based on these spatially independent datasets. The rms errors of the predicted broadband reflectance are found to be 1.0, 1.8, 2.0, and 3.1 for the ocean, land, ice–snow, and cloud data, respectively. The effects of scene discrimination and solar and viewing geometry on the regressions are investigated, and comparisons are made between two-channel and single-channel models. The use of two solar channels is found to give a significant improvement in the predicted broadband reflectance for datasets in which there is no scene discrimination, a small improvement for measurements over land, and no improvement for the other homogeneous scene types. Geometric factors are found to have no significant effect on the regressions.

1. Introduction

With the prime purpose of providing cloud imagery for weather analysis and forecasting, operational satellites have provided continuous coverage of the earth for more than 30 years and will undoubtedly continue to do so. Though the observations are limited to narrow spectral intervals, their use for estimating radiation budgets both at the top of atmosphere and at the earth's surface has been attempted extensively on the basis of the correlation between narrowband and broadband radiances (Gautier et al. 1980; Gruber et al. 1983; Nunez et al. 1984; Dedieu et al. 1987). All of the investigations were based on the very crude assumption that the visible albedo is equal to the total albedo. Despite this, some results have proved to be useful for a variety of problems in climate studies (Ohring and Gruber 1983), since the narrowband data comprise the longest continuous dataset over the globe with high and homogeneous resolution. However, as pointed out by Stowe (1988), successful monitoring and modeling of the earth's climate requires that high-quality broadband measurements of the earth's radiation budget (ERB) be made on a continuous basis for at least several decades. Measurement programs, such as those by *Nimbus-7* and the Earth Radiation Budget Experiment (ERBE), have begun to address this problem, but these programs were experimental and of limited term and there is no plan to recommence broadband measurements until the latter part of this decade. It is because of this problem that Stowe suggested that estimates of broadband fluxes from narrowband data should serve as surrogate broadband data to fill gaps in the time record of broadband measurements. To achieve these objectives, modeling and empirical studies are needed to elucidate the factors that govern the relationship between narrowband and broadband fluxes.

In theoretical studies, the conversion from narrowband to broadband quantities is typically accomplished by incorporating the narrowband filter functions into an atmospheric radiation model and then performing numerical simulations for a wide variety of atmospheric conditions and surface types. The model results serve as a database upon which regressional analysis is conducted (Stum et al. 1985; Cess and Potter 1986; Pinker and Ewing 1986, 1987; Ellingson et al. 1989). However, as pointed out by Davis et al. (1984), not only is it an ambitious task to utilize a full-fledged radiative transfer model for such a large number of simulations, it is

Corresponding author address: Dr. H. G. Leighton, McGill University, Department of Meteorology, 805 Sherbrooke Street West, Montreal, Quebec H3A 2K6, Canada.

difficult to capture in the simulated data realistic variabilities of water vapor amounts, clouds, surface anisotropy, etc. Therefore, the simulated data may not represent conditions that are typical of those that actually exist.

Alternatively, regressional equations may be derived from actual coincident measurements of narrowband and broadband reflectances. Minnis and Harrison (1984), for example, matched *Nimbus-7* ERB shortwave radiometer data with GOES visible measurements (0.55–0.75 μm), obtaining quadratic regressional equations for land, ocean, and clouds. A pair of narrowband and broadband measurements was considered as being quasi-simultaneous and quasi-collocated if they were made within 15 min of each other and if the solar zenith angle, viewing zenith angle, and relative azimuth angle between two measurements differed by less than 2.5°, 7.5°, and 15°, respectively. Wydick et *Nimbus-7* ERB broadband data and *NOAA-7* Advanced Very High-Resolution Radiometer (AVHRR) narrowband data in channels 1 (0.58–0.68 μm) and 2 (0.72–1.10 μm). Since the narrowband and broadband measurements were made from different spacecraft flying in different orbits, the number of matching data pairs was limited.

ERBE broadband measurements and AVHRR narrowband measurements from *NOAA-9* are ideally suited to address this problem, since both sets of radiometers are aboard the same spacecraft and scan in a similar mode across the satellite track. The rate of collection of data from collocated, coincident ERBE and AVHRR pixels is very much larger than is the case when the instruments are mounted on different spacecraft, and thus adequate statistics may be obtained from only a few days of data. In order to optimize the narrowband to broadband conversion, the data are usually grouped according to scene type. In this respect, AVHRR data have an additional advantage compared to the previously cited approaches in that multichannel AVHRR data are more suitable for scene identification. In this study we are concerned with radiation budgets at high latitudes, and therefore scene types are determined from algorithms previously developed for this purpose (Sakellariou and Leighton 1988; Sakellariou et al. 1990; Li and Leighton 1991). As pointed out by Payette (1989), radiances from neighboring pixels are highly correlated. This correlation must be accounted for in the regression analysis. An objective sampling method is described that ensures only spatially independent data are included in the analysis.

The particular problems associated with the application of regressional methods to spatially autocorrelated data and an approach to the solutions of these problems are introduced in section 2. Section 3 presents autocorrelation analyses of the measured reflectances. Some screening constraints and a sampling method based on the autocorrelation analyses are proposed in section 4. The regression analyses that relate broadband and narrowband reflectances are given in section 5. The results are summarized in section 6.

2. Spatial autocorrelation and regression analysis

Classical regressional analyses based on least-squares estimation were used in all the previously cited studies that empirically determined the relationship between narrowband and broadband reflectances or albedos. One of the inherent assumptions of this approach is that the residuals from the regression are independent. A failure to comply with this requirement may have several effects on the regression analysis. First, use of an ordinary least-squares (OLS) method will yield inefficient estimates of the regression coefficients in the sense that they no longer generate minimum variance. Second, the estimates of confidence intervals and the various tests of significance commonly employed would no longer be valid. Third, the estimate of the standard errors of the regression may be seriously underestimated, leading to a spurious impression of accuracy (Chatterjee 1977; Miron 1984). The assumption of independence among the residuals is especially likely to be violated in such highly spatially autocorrelated data as are obtained from satellite measurements. Preliminary studies of the spatial autocorrelation among ERBE measurements suggested that observations should be separated by about 2000 km to be completely independent of each other (Payette 1989).

To characterize the spatial dependence, certain statistics known as spatial autocorrelation are necessary to provide basic information about the distribution of the data that is not available from other descriptive statistics such as the mean and variance. Autocorrelation statistics provide a numerical summary about how the data are arranged in the space in a form that is useful for statistical testing. Unlike the mean and variance, autocorrelation statistics are not only functions of the data values but are also functions of the arrangement of those values in space. The arrangement is described by a so-called weighting function that assigns values to pairs of locations that depend on their arrangement in space (Odland 1988).

One of the autocorrelation statistics specifically designed for testing hypotheses of spatial dependence is called Moran's I (Cliff and Ord 1973), defined as

$$I = \frac{\sum_{i=1}^{n}\sum_{j=1}^{n} w_{ij}(x_i - \bar{x})(x_j - \bar{x})}{[(1/n)\sum_{i=1}^{n}\sum_{j=1}^{n} w_{ij}][\sum_{i=1}^{n}(x_i - \bar{x})^2]}, \quad (1)$$

where x_i and x_j are values of the variable X in a pair of regions i and j, n is the sample size, and w_{ij} is a weighting function. In fact, Moran's I is just a correlation coefficient between the weights w_{ij} and the individual cross products $X_{ij} = (x_i - \bar{x})(x_j - \bar{x})$, since

the numerator is their covariance and the denominators are the appropriate normalizing factors. Thus, Moran's I is a means of comparing w_{ij} and X_{ij} to ascertain if patterns of variation in the cross product are similar to patterns of variation in the weight (Odland 1988). A suitable weighting function should be able to characterize the variation of the cross product over space. Choosing an appropriate weighting function depends both on a priori physical considerations and on the analysis of the autocorrelation of the cross product over space. For certain applications it can be as simple as a one or zero step function; that is, $w_{ij} = 1$ if i and j are neighbors and 0 otherwise. The distance between two measurements of reflectance is a major factor that influences their correlation. The particular form of the weighting function for the present data will be given in the following section.

As in classical hypothesis testing, tests for spatial autocorrelation require knowledge of the statistical distribution of the selected statistic under the null hypothesis of random and independent distribution of the data in space. The test of spatial autocorrelation is based on the comparison between the value of the autocorrelation statistic calculated from the samples and the theoretical value expected under null hypothesis. While there are many forms of spatial autocorrelation statistics, only a few, including Moran's I, have well-defined distributional properties that make it possible to use them in conventional statistical tests. A major contribution of Cliff and Ord (1973) has been a thorough specification of the distributional properties of Moran's I. Moran's I was proved to be asymptotically normally distributed as n increases, with mean and variance for randomly distributed data given by

$$E(I) = -\frac{1}{n-1} \tag{2}$$

$$\text{var}(I) = \frac{n^2 S_1 - nS_2 + 3(\sum_{i=1}^{n}\sum_{j=2}^{n} w_{ij})}{(\sum_{i=1}^{n}\sum_{j=1}^{n} w_{ij})^2 (n^2-1)}, \tag{3}$$

where

$$S_1 = 0.5 \sum_{i=1}^{n}\sum_{j=1}^{n} (w_{ij} + w_{ji})^2 \tag{4}$$

$$S_2 = \sum_{i=1}^{n} (\sum_{j=1}^{n} w_{ij} + \sum_{j=1}^{n} w_{ji})^2. \tag{5}$$

Provided that the appropriate weighting function is selected, it follows from (2) that the expected value of I for data that is not spatially correlated approaches 0 as the number of observations increases. If n is not too small, positive and negative values of I indicate that the variable under study is, respectively, positively or negatively autocorrelated. For w_{ij} symmetric with respect to i and j, the expressions for S_1 and S_2 simplify to

$$S_1 = 2 \sum_{i=1}^{n}\sum_{j=1}^{n} w_{ij}^2 \tag{6}$$

$$S_2 = 4 \sum_{i=1}^{n} (\sum_{j=1}^{n} w_{ij})^2. \tag{7}$$

Based on these parameters, significance tests can be performed against a null hypothesis that the data are not spatially correlated. More specifically, the calculated value of I should be equal to $E(I)$ within the limits of statistical significance if the data are spatially independent. If the calculated value exceeds $E(I)$ significantly, then the x_i are spatially dependent.

In addition to having well-defined statistical properties, Moran's I has the feature of not requiring the data to be equally spaced or continuous. This is of special importance here, since after being subjected to several constraints and sampling as discussed in section 4 the data used in the regressional analysis may be distributed quite irregularly.

If the spatial autocorrelation is found to be significant, a simple solution is to remove the spatial autocorrelation by selecting a sampled subset of the data, thus allowing application of a classical regressional analysis (Cliff and Ord 1981). The use of Moran's I provides a convenient and objective sampling strategy.

In the following section, spatial autocorrelation analyses, or correlogram analyses, are employed to determine the weighting function to be used in the calculation of Moran's I and also to determine the sampling scheme.

3. Correlogram analysis

A correlogram is a graph of the variation of autocorrelation coefficient with spatial lag. Correlogram analyses of shortwave and longwave ERBE radiances measured at low latitudes were conducted by Payette (1989). The values of the autocorrelation coefficients are closely related to the radiative features specific to the region and season under study. Both the cloud climatology and underlying surface types at low latitudes are quite different from those at high latitudes; this will lead to different spatial characteristics of the reflectance in the two regions.

The spatial autocorrelation coefficient ρ is defined as the ratio of the autocovariance or cross product divided by the variance

$$\rho(i, m) = \frac{c(i, m)}{\sigma^2(i)} \tag{8}$$

$$c(i, m) = \begin{cases} \dfrac{1}{n-m} \displaystyle\sum_{j=1}^{n-m} (R_{i,j} - \bar{R}_i)(R_{i,j+m} - \bar{R}_i) & \text{along track} \\ \dfrac{1}{n} \displaystyle\sum_{j=1}^{n} (R_{i,j} - \bar{R}_i)(R_{i+m,j} - \bar{R}_{i+m}) & \text{across track} \end{cases} \tag{9}$$

$$\sigma^2(i) = \frac{1}{n}\sum_{j=1}^{n}(R_{i,j} - \bar{R}_i)^2 \qquad (10)$$

$$\bar{R}_{i+m} = \frac{1}{n}\sum_{j=1}^{n} R_{i+m,j}, \qquad (11)$$

where R denotes the reflectance and subscript, i the position of the initial pixel across the track, j the pixel position along the track, m the lag, and n the number of scan lines.

The autocorrelation coefficient $\rho(i, m)$ ranges from -1 to 1. The spatial lag may be expressed either in terms of distance or pixel number. Since the dimensions of pixels are different in the along- and across-track directions, the spatial autocorrelation coefficients expressed in terms of pixel number will be different in the two directions. Furthermore, since the pixel dimensions vary with viewing zenith angle, the autocorrelation coefficient for a particular lag expressed in terms of numbers of pixels will depend on the initial pixel position. Accordingly, the autocorrelation coefficients are calculated as functions of the lag for different across-track positions of the initial pixel. From each across-track scan and for each value of m, two pairs of points are obtained, the initial pixel in each pair being located symmetrically on either side of nadir. For the initial pixel at nadir, the two pairs are obtained by selecting the lagged pixels located m pixels to the left and right of nadir. For the initial pixel off nadir, one pair is obtained by selecting the initial pixel to the left of nadir and the lagged pixel to the right of the initial pixel and the other by selecting the initial pixel to the right of nadir and the lagged pixel to the left of the initial pixel (Fig. 1). Thus, pairs of pixels with the same displacement from nadir and same lag expressed in numbers of pixels have the same actual separation.

The data that are subjected to the correlogram analysis are ERBE broadband shortwave radiances from all passes on 1, 10, 19, and 29 July 1985 in the region north of 60°N for solar zenith angles smaller than 82°. For each day there are approximately 14 passes, each pass containing 220 ERBE scan lines. There are 62 pixels in each ERBE scan line, but near the edges of each scan there are always a few pixels that are flagged as having unreliable measurements. For the sake of uniformity, only the 51 pixels closest to nadir are included in the analysis. The largest across-track lag that is considered is 25 pixels. Although correlation coefficients along the track could be calculated for lags as large as 220 pixels, the sample size for these long lags would be small, and hence the autocorrelation coefficient along the track is calculated for a maximum lag of 30 pixels.

Figure 2 shows the autocorrelation coefficients plotted against centroid-to-centroid distance for the complete dataset (5.5×10^5 pixels). The autocorrelation coefficient decays gradually to a value of about 0.2 at

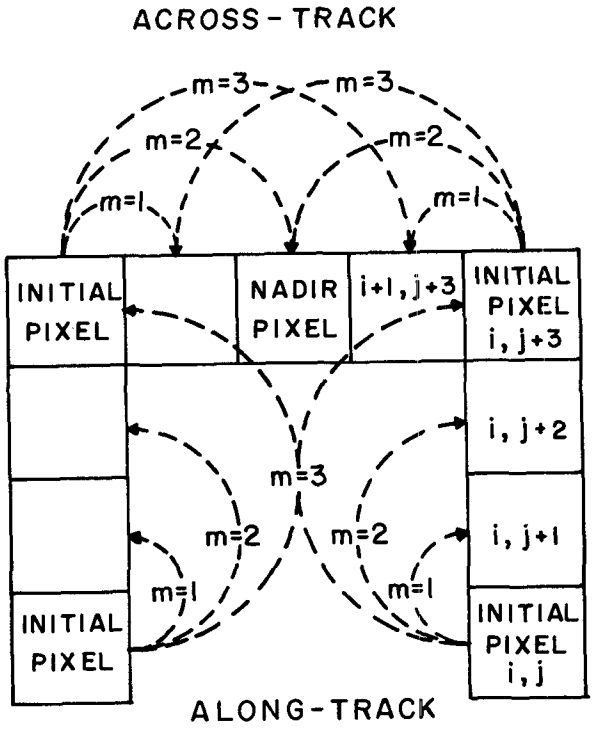

FIG. 1. Diagram showing the selection of pixel pairs for along- and across-track autocorrelation analyses. The position of pixels across and along the satellite track are indicated by i and j, respectively. The number of lagged pixels is denoted by m.

800 km, confirming the observations of Payette (1989) that measurements separated by a few hundred kilometers cannot be treated as independent samples. It is also evident that the autocorrelation coefficients computed along and across the satellite track are very similar. As indicated by the solid line, they can be expressed as a simple exponential function of the form

$$\rho_{ij} = 1.0021^{-d_{ij}}, \qquad (12)$$

where d_{ij} is the separation in kilometers between pixels i and j. Since this function describes the spatial pattern of the autocorrelation so well, it is selected as the weighting function for the calculation of Moran's I; that is,

$$w_{ij} = \rho_{ij}. \qquad (13)$$

In order to establish a suitable scheme to sample the complete dataset, information is needed on the variation of the spatial autocorrelation coefficient with lagged pixel number rather than distance.

Figure 3 shows the autocorrelation coefficients plotted against the number of lagged pixels along the track for various across-track locations. The line numbers denote the across-track positions where the along-track autocorrelation coefficients were calculated, 1 representing along track at nadir and 2, 3, 4, 5, and 6 denoting positions that are 5, 10, 15, 20, and 25 pixels

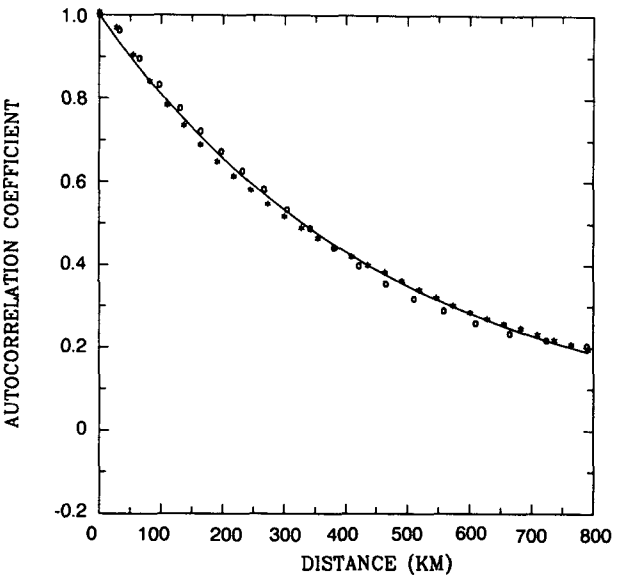

FIG. 2. Autocorrelation coefficient ρ as a function of lagged distance d along (*) and across (O) the satellite track. The curve shows the fit to the data points given by the function $\rho = 1.0021^{-d}$. Data are from all passes on 1, 10, 19, and 29 July 1985 in the region north of 60°N.

away from nadir, respectively. A comparison of the various curves shows no substantial difference in along-track coefficient with across-track position as long as the displacement from nadir is less than 20 pixels (line 5), corresponding to a viewing zenith angle of 52°. At viewing zenith angles larger than this, the relatively large pixel size seems to be responsible for a more gradual decrease of autocorrelation. The spread between curves 1 to 5 may be taken as a measure of the upper limit of the uncertainty in the value of ρ.

Shown in Fig. 4 are the across-track correlograms for different positions of the initial pixel. The considerable differences between the various curves show that the autocorrelation coefficient depends not only on the lag expressed in terms of numbers of pixels but also on the initial position. The autocorrelation coefficients with origin near the edges of a swath decay very quickly for the first few lagged pixels and then more and more slowly. In comparison, the coefficients calculated for an origin near nadir decrease fairly uniformly. These differences are easily explained in terms of changes in centroid-to-centroid distances between pixels for different pixel locations.

The variation of the autocorrelation coefficient with lagged pixel number n can also be expressed as an exponential function

$$\rho = \alpha^{-n}. \tag{14}$$

Figure 5 shows exponential fits to the along- and across-track autocorrelation data that comprise lines 1 and 6 in Figs. 3 and 4. The values of α range from 1.08 to 1.27 for the across-track coefficients and from 1.03 to 1.06 for along-track coefficients.

4. Data for narrowband to broadband conversion

a. Match-up of AVHRR and ERBE measurements

From the latitude and longitude information contained in both the AVHRR global area coverage (GAC)

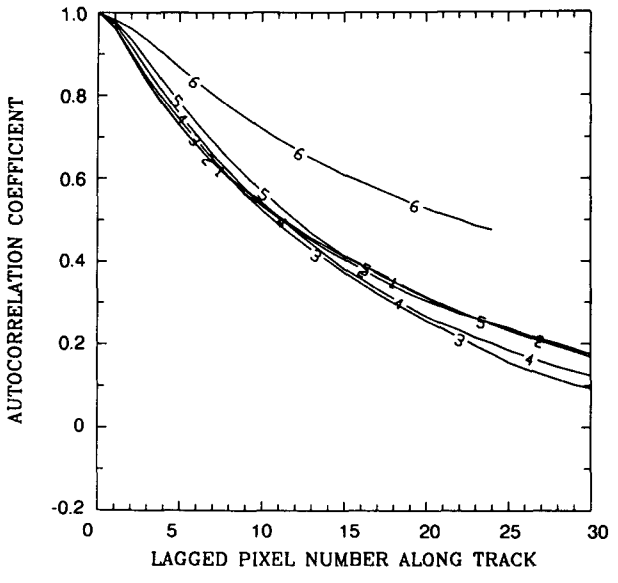

FIG. 3. Autocorrelation coefficient versus lagged pixel number along the satellite track calculated at different initial positions across the track. The lines numbered 1, 2, 3, 4, 5, and 6 are for initial pixels 0, 5, 10, 15, 20, and 25 pixels away from the nadir, respectively.

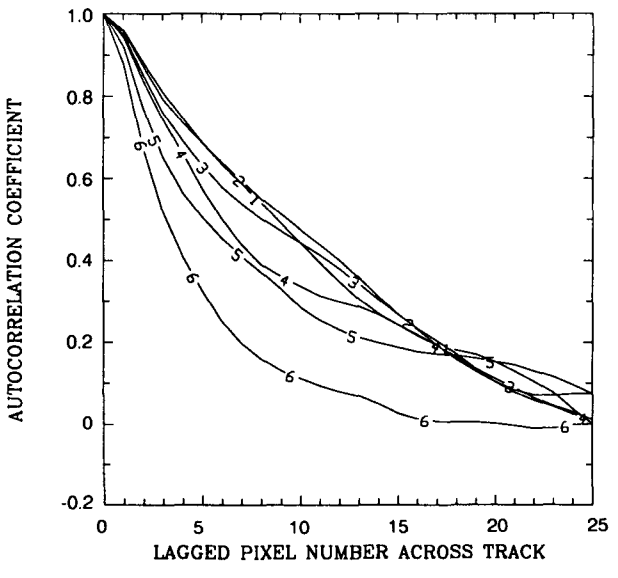

FIG. 4. Same as Fig. 3, but with lags taken across the satellite track.

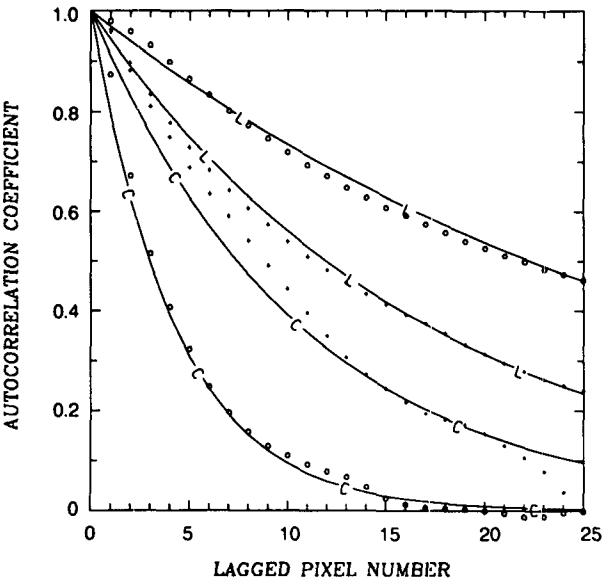

FIG. 5. Fits to the along-track (L) and across-track (C) autocorrelation coefficients at nadir (+) and 25 pixels away from nadir (○). The curves have the form $\rho = \alpha^{-N}$, where N is the pixel lag.

and ERBE datasets, the AVHRR pixel that is closest to the center of each ERBE pixel is identified. The distance between the centers of the AVHRR pixel and the ERBE pixel is generally less than 2 km, but if it is greater than 5 km the ERBE data is flagged and not used. The array of 8 × 8 AVHRR (GAC) pixels centered on the closest pixel is assumed to correspond to the ERBE pixel.

b. *Scene identification*

Separate conversion functions are required for each distinct scene type. For the region of interest in this work, the relevant scene types are ocean, land, ice/snow, and cloud. Because of the difficulty in distinguishing between cloud and snow- and ice-covered surfaces on the basis of broadband shortwave and longwave radiances, ERBE identified scene types are not reliable for this region (Li and Leighton 1991). Scene type corresponding to an ERBE field of view is determined by applying the method of Sakellariou et al. (1992) to the 64 AVHRR pixels that correspond in the manner described above to each ERBE pixel. If 95% (i.e., 58) or more of the AVHRR pixels are found to be cloudy, the ERBE pixel is classified as being overcast. If 95% or more of the pixels are clear ocean, land, or snow/ice, the ERBE pixel is classified as being clear and of the appropriate surface type; otherwise the ERBE pixel is discarded.

c. *Homogeneity constraint*

After scene identification, a homogeneity constraint is applied. For each array of 64 AVHRR pixels matched to an ERBE pixel, the dispersions of the radiances in channels 1 and 2, defined as the ratio of the standard deviation to the mean, are calculated. In order to impose an even greater degree of homogeneity on the ERBE pixels than is required in the scene identification step, only pixels for which the dispersions in both channels are less than 0.1 are retained. This procedure resulted in the rejection of 62%, 68%, 65%, and 72% of the ocean, ice, land, and overcast pixels in the sampled datasets, respectively. Imposition of this condition increases the probability that the scene is uniform, eliminates the need for the application of the ERBE point spread function to the AVHRR radiances to obtain an appropriately weighted mean AVHRR radiance over the ERBE pixel, and reduces sensitivity to geographic matching errors.

d. *Sampling*

The sampling procedure is designed to be objective, simple to implement, and efficient. It involves a trial and error approach in which the full dataset is first sampled with the requirement that the sampled data have an autocorrelation less than some large initial value of ρ. The sampled data are then subjected to the scene identification and homogeneity constraints. Moran's I is computed for the sampled, homogeneous, single scene-type data and tested against the null hypothesis that the data are spatially independent. If the hypothesis is rejected, a smaller value of the autocorrelation coefficient is selected and the procedure repeated. The decision to reject or accept the hypothesis is made by determining whether the calculated standard normal deviation defined by

$$D = \frac{I - E(I)}{[\mathrm{var}(I)]^{1/2}} \tag{15}$$

exceeds the theoretical value D_α obtained from a normal probability distribution at significance level 0.05. If $D > D_\alpha$, the assumption of spatial independence is rejected; otherwise the dependence is not significant.

Because of the differences in the along- and across-track corellograms, the sampling procedure is different in the two directions. Account must also be taken of the variations of the across-track autocorrelation coefficient with initial pixel position. Shown in Fig. 6 are contours of the across-track autocorrelation coefficient plotted as functions of initial pixel position and across-track lag. The number of pixels to be skipped after each pixel is selected is determined by the pixel position and the chosen value of ρ. For example, if pixels are to be selected with an autocorrelation coefficient of 0.6 by following the $\rho = 0.6$ contour starting from the right edge of the scan, the sampled pixels would be 25, 23, 20, 17, 13, 8, and 2 pixels to the right of nadir and continuing with pixels displaced to the left of nadir by 5, 12, 17, 21, and 24 pixels. In order that pixels at all

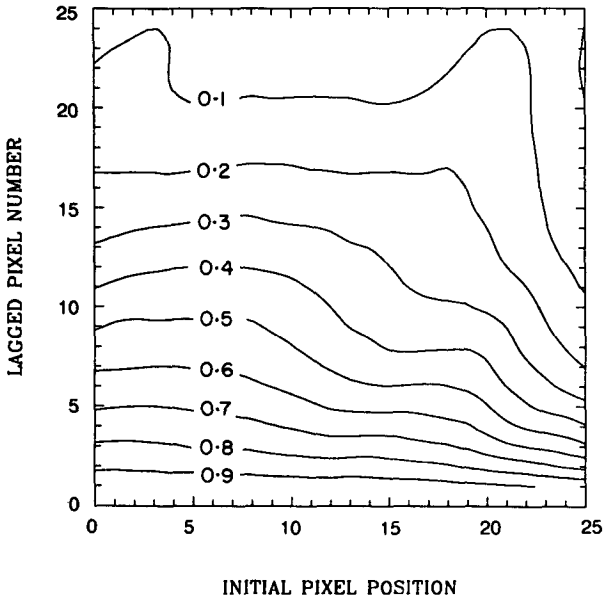

FIG. 6. Contour map of across-track autocorrelation coefficient as a function of lagged pixel number and initial pixel position relative to nadir.

viewing zenith angles may be selected, the first pixel to be sampled from successive scan lines cycles periodically with a step of one pixel from pixel 25 to pixel 20. That is, if the first pixel selected from a particular scan line is pixel 25 on the right of nadir, on the next scan line it will be pixel 24 on the left of nadir and so on to pixel 20, after which the cycle recommences with pixel 25. Due to the small variability of the along-track autocorrelation coefficient with an initial position across track, the number of scan lines that is skipped is kept constant at the number determined by the value of ρ at nadir.

It was found that applying this procedure with an autocorrelation coefficient of 0.4 produced datasets for each scene type that were spatially independent at a confidence level of 95% according to significance tests based on Moran's I. It should be noted that the selected value of ρ of 0.4 is a measure of the autocorrelation of the data before being subjected to the constraints, it is not a measure of the autocorrelation of the sampled, homogeneous datasets.

In addition to spatial sampling, temporal sampling was also imposed by only selecting data from every second satellite pass. Figure 7 shows the geographical

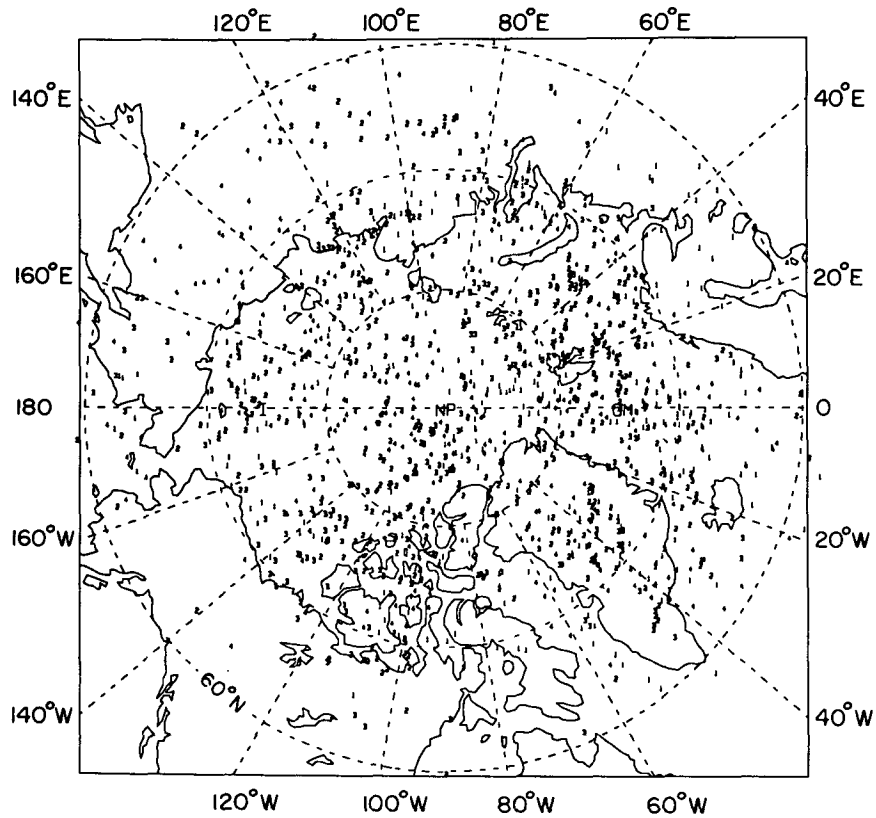

FIG. 7. Geographic distribution of cloudy pixels used for the regression analysis, after scene discrimination, homogeneity screening, and sampling. The symbols 1, 2, 3, and 4 indicate data from 1, 10, 19, and 29 July 1985, respectively.

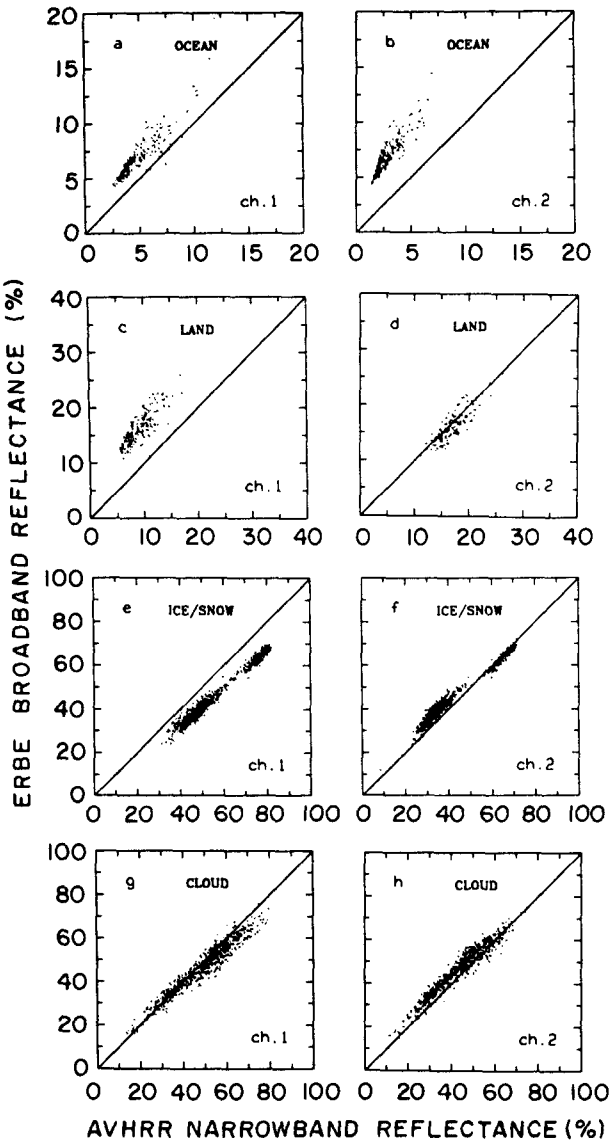

FIG. 8. Scattergrams of simultaneous and coincident ERBE broadband and AVHRR narrowband reflectances for ocean, land, ice/snow, and cloud pixels. Left and right panels correspond to channel 1 and 2 of AVHRR, respectively.

distribution of the data finally used in the regression analysis for overcast pixels. It is significant that the data from each of the 4 days are homogeneously distributed over the domain and most importantly that there is no discernible cluster.

5. Regression analysis

a. Development of the regression models

After being subjected to the screening constraints and the spatial and temporal sampling described above, the sizes of the ocean, land, ice–snow, and overcast datasets are 541, 555, 2040, and 1528 pixels, respectively. Scatter diagrams of simultaneous and coincident ERBE broadband and AVHRR narrowband reflectances in channels 1 and 2 are plotted in Fig. 8 for the four pure scene types. Although the relationships between broadband and narrowband reflectance are quite different for the four scene types, for single scene types there appears to be a strong linear relationship between broadband R_b and narrowband reflectances R_1 and R_2 in channels 1 and 2 of the AVHRR. This suggests the following simple model to estimate broadband reflectance:

$$R_b = a + b_1 R_1 + b_2 R_2. \qquad (16)$$

The coefficients determined from bivariate regression analyses of measurements made on 1, 10, and 29 July are given in Table 1, together with measures of the regression errors. Measurements made on 19 July serve as an independent dataset to test the model. Also included in Table 1 are results of the regression analysis of the dataset consisting of the combination of the four individual datasets; that is, with no discrimination according to scene type.

It is evident that a very good fit is achieved for ice/snow with about 97% of the variance of the broadband reflectance being explained by the regression model. The rms error and the relative error of the broadband estimates are 1.8% and 4.5%, respectively. The cloud model also performs well as is indicated by the explained variance of 93% and relative error of 6.5%.

TABLE 1. Summary of statistics from the regression analyses with the two-channel model for the estimation of broadband reflectance based on ERBE and AVHRR data from 1, 10, and 29 July 1985. Except for b_1 and b_2, all the values are given in percent.

Scene	Sample size	Coefficients			Explained variance	rms error	Relative error*
		a	b_1	b_2			
Ocean	401	2.48	0.490	0.699	82.6	1.0	13.8
Land	423	1.25	0.673	0.518	76.7	1.8	10.4
Ice/snow	1514	4.53	0.389	0.452	97.2	2.0	4.5
Clouds	1140	6.98	0.410	0.448	92.8	3.1	6.5
All	3478	4.42	0.287	0.607	97.7	2.7	7.1

* Relative error is defined as the ratio of rms error over the mean measured broadband reflectance.

These results are not surprising if one notes the good linear relationship between narrowband and broadband reflectances in Figs. 8e–h. The large spreads in Figs. 8a–d lead to relatively poor estimates of broadband reflectance for ocean and land scenes as is evident from the small value of the explained variance and large relative error. The poor performance of regression model over land is mainly due to the strong spectral dependence of reflectance on vegetation type (Cess and Vulis 1989). The cause of the lower predictability of broadband reflectance over ocean might be due in part to the greater significance of variability of the atmospheric radiative properties when the surface reflectance is small. Regression analysis by Davis et al. (1984) based on simulated data also show that regression models for snow are better than those for water and land. The present results may also be compared with results based on *Nimbus-7* and *NOAA-7* data reported by Wydick et al. (1987). For similar regression models, they obtained rms errors of 1.4%, 2.1%, 4.6%, and 7.5% for ocean, land, snow, and cloud, respectively. These values are significantly higher than those from the present study, especially for ice/snow and clouds. This can be attributed to their less accurate spatial matching of the narrowband and broadband measurements and the relatively large field of view of the *Nimbus-7* radiometer compared to the ERBE radiometer. Furthermore, the values of rms error given by Wydick et al. (1987) are most probably underestimated, since their data are likely to have had significant spatial correlation.

To see the impact of spatial autocorrelation on the regression results, the same regression analysis is applied to the data that are obtained without the sampling procedure but with the other constraints. The explained variances for the measurements of ocean, land, ice/snow, and clouds are 60.4%, 73.8%, 96.8%, and 85.4%, respectively. It should be noted that when the samples are not independent, only the explained variance is a valid measure of the goodness of fit. Both the rms error and relative error tend to be underestimated because they depend on the number of degrees of freedom, which is not equal to, but is significantly smaller than, the number of measurements (Cliff and Ord 1981). Compared with the explained variances presented in Table 1, it is found the regression based on independent data is much better than that based on the unsampled dependent data. This is not surprising, since, as discussed in section 2, OLS is no longer a valid procedure to obtain the minimum variance.

Comparisons of observed and predicted broadband reflectances for the datasets that are used to generate the regression models are shown in Fig. 9. The absence of systematic deviations between predicted and observed reflectance suggests that the least-squares analysis is valid and that the linear relationship given by (16) is appropriate. A similar comparison, but for the independent test datasets from 19 July, gave results

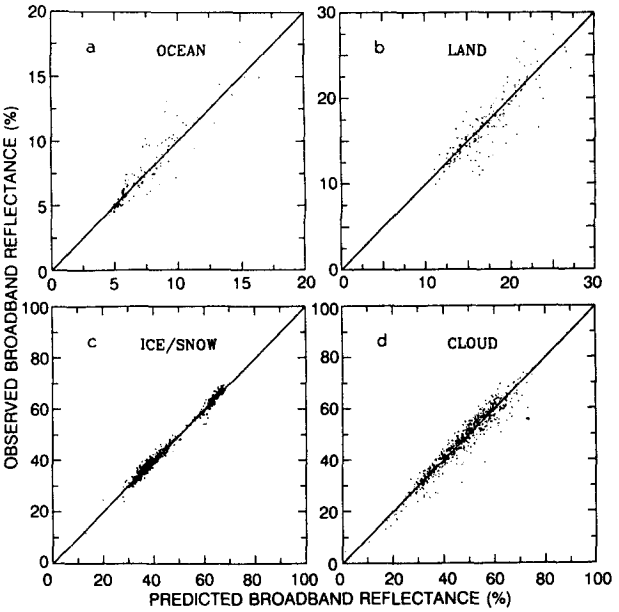

FIG. 9. Comparisons of observed and predicted broadband reflectances for data used to determine the regressions: (a) ocean, (b) land, (c) ice/snow, (d) cloud. Data are from 1, 10, and 29 July 1985.

that were essentially identical in pattern and in magnitude. The rms errors for the independent datasets are 1.1%, 2.1%, 1.9%, and 3.0% for ocean, land, ice/snow, and cloud, respectively. This suggests that the size of the datasets used to develop the regression models is large enough to provide stable regression coefficients. If the regression models derived from the unsampled data are applied to the same independent data, the rms errors are 1.8%, 3.0%, 2.5%, and 4.6% for ocean, land, ice/snow, and cloud, respectively. These values are significantly larger than those obtained from the regression model based on the sampled independent data.

b. Effects of scene discrimination

Several investigators (e.g., Davis et al. 1984; Pinker and Ewing 1987) have argued that scene discrimination is crucial if one is to be able to accurately estimate broadband reflectance from narrowband measurements. On the other hand, the studies of Wydick et al. (1987) drew a quite different conclusion. They found that the accuracy of broadband reflectance estimation without scene-type discrimination was similar to that for individual scenes in terms of rms error and even better in terms of explained variance. This is confirmed by the present results shown in Table 1. Figure 10 presents a scattergram of broadband and narrowband reflectances for the combination of the four individual datasets that comprise Fig. 8. Although there is a much larger spread than is found for any of the pure scenes, as is clear from the last line of Table 1 and Fig. 11, the

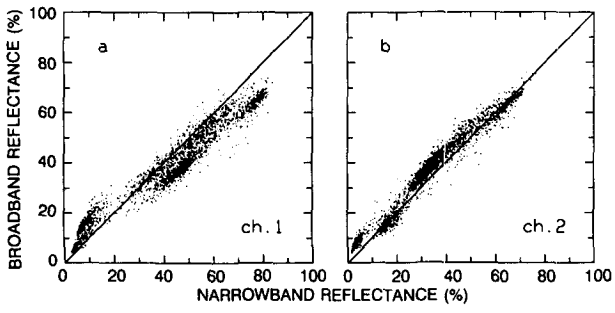

FIG. 10. Combined scattergram of data from all four scene types of broadband and narrowband reflectance in (a) channel 1 and (b) channel 2. Data are from 1, 10, and 29 July 1985.

two-channel scene-independent model is able to give good predictions of broadband reflectance. It would, however, be a mistake to conclude that scene discrimination is unimportant in deducing broadband reflectances from narrowband measurements, since, as is illustrated in Fig. 12, systematic errors are observed when the scene-independent model is applied to homogeneous scenes.

c. *Contribution of channel 2*

Several previous studies have used single-channel narrowband solar reflectance measurements to deduce the broadband reflectance. For example, Gruber et al. (1983) used channel 1 data from the AVHRR and Minnis and Harrison (1984) used GOES visible data. To assess the benefits of including information from both channels 1 and 2 of the AVHRR in the regressions, the analyses were repeated using only channel 1 reflectances.

Table 2 presents a summary of the statistics from the regression analyses based on channel 1 of the AVHRR. Except for land, the explained variance from the single-channel regression is almost as large as when both channels 1 and 2 are used. This is a consequence of the strong correlation between the two channels for ocean, ice/snow, and cloud (Fig. 13). Of more significance are the differences in rms errors between the single-channel and two-channel analyses that are small for all the pure scenes but significantly larger for the combined scenes. This suggests that if scene types are differentiated, there is little advantage to using both AVHRR shortwave channels to deduce broadband reflectance. However, if scene type is not identified, better estimates of broadband reflectance may be obtained from the use of both AVHRR shortwave channels.

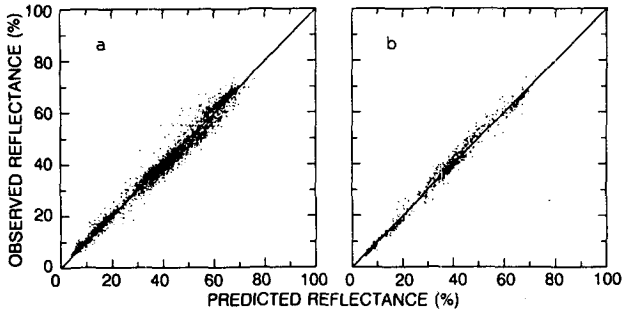

FIG. 11. Comparison of observed and predicted broadband reflectances for the combined data. (a) Data from 1, 10, and 29 July used to determine the scene-independent regression; (b) independent test data from 19 July 1985.

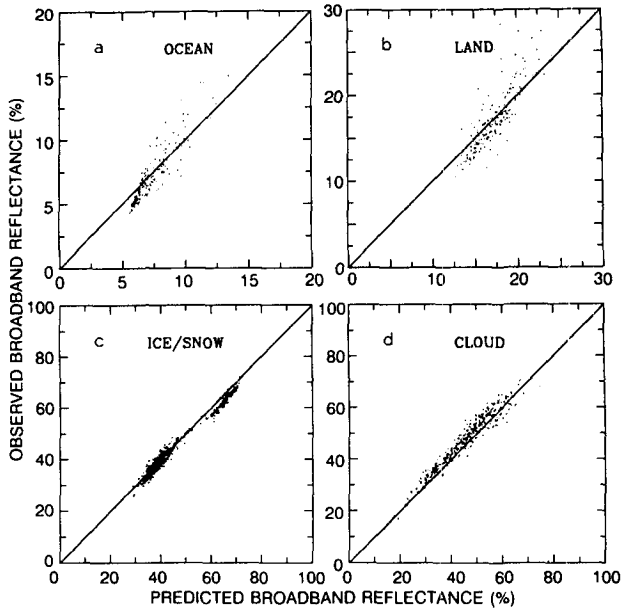

FIG. 12. Same as Fig. 9, but using the scene-independent regression.

d. *Effects of geometric factors on the regression coefficients*

It may be expected that differences in the anisotropy of narrowband and broadband reflectances will lead to the dependence of the regression coefficients on geometric factors. Davis et al. (1984) found from their simulation studies that the regression coefficients were insensitive to the solar and viewing geometry. However, theoretical studies by Stum et al. (1985) show a significant dependence of the narrowband to broadband

TABLE 2. Summary of statistics from the regression analyses with the single-channel model for the estimation of broadband reflectance based on the ERBE and AVHRR data from 1, 10, and 29 July 1985.

Scene	Coefficients		Explained variance	rms error	Relative error
	a	*b*			
Ocean	1.92	1.025	81.6	1.1	14.2
Land	6.93	1.014	63.5	2.2	13.0
Ice/snow	−1.94	0.855	96.4	2.3	5.1
Clouds	6.44	0.822	91.7	3.3	7.0
All	5.75	0.767	94.5	4.2	11.0

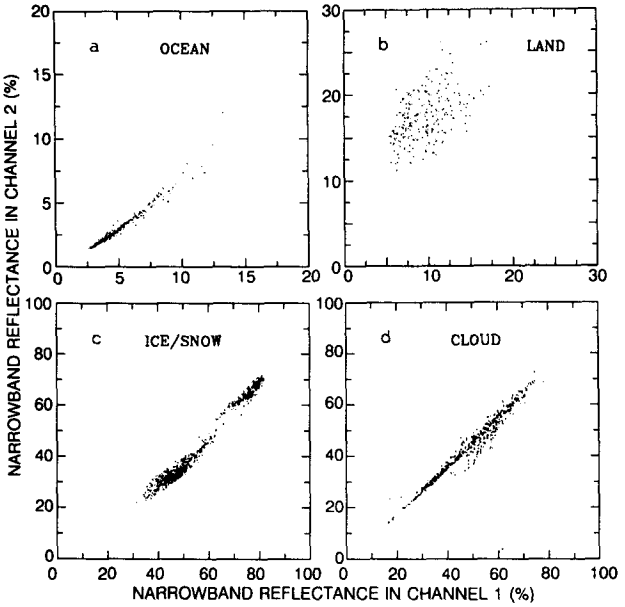

FIG. 13. Relationships between narrowband reflectances in channel 1 and channel 2 of the AVHRR.

conversion factor on the viewing and solar zenith angles. Until now, no attempt has been made to address this problem empirically because of the lack of appropriate data. The present datasets contain the values of the solar and viewing zenith angles and the relative azimuths and thus are convenient to study the effects of geometric parameters on the narrowband to broadband conversions. In the present data, solar zenith angles are greater than 40° and viewing zenith angles are less than 70°. Limitations on the range of relative azimuth angles experienced in the sun-synchronous satellite orbit prevent studying its effect on the conversions.

The azimuth-averaged bidirectional reflectance can be expressed as a polynomial of low order of the parameter μ^* defined by

$$\mu^* = \frac{\mu\mu_0}{\mu + \mu_0}, \tag{17}$$

where μ and μ_0 are cosines of viewing zenith angle and solar zenith angle, respectively (Staylar 1985; Staylor and Suttles 1986; Vulis and Cess 1989). Accordingly, each coefficient in (16) is expressed in the form

$$a_i = c_0 + c_1\mu^* + c_2\mu^{*2}. \tag{18}$$

After expressions of the form given by (18) are substituted into (16), new regression analyses are conducted. Though reductions in the rms errors are found, the improvements are so small that they cannot be considered to be significant. Other functional forms for the zenith-angle dependence were also tested, but none produced significant reductions in errors.

6. Summary

Due to their temporal continuity and global coverage, AVHRR measurements can be of special importance in climate studies. However, broadband radiation observations are more useful than narrowband measurements such as those from the AVHRR. While regressional models to convert narrowband to broadband reflectances have been developed from previous empirical studies, they all suffer two major shortcomings. One is that there are large errors in the matching of broadband and narrowband measurements made from different satellites. The coincident and simultaneous ERBE and AVHRR measurements made from the operational polar-orbiting satellites such as *NOAA-9* largely overcome this problem. Another common drawback is the neglect of spatial dependence among the residuals. Residual independence is a basic assumption that a conventional regressional model must fulfill in order to correctly obtain regression coefficients and estimates of regressional errors by means of the classical least-squares estimator. A strong spatial dependence among residuals will exist from a regression based on highly spatially autocorrelated satellite measurements made by scanning radiometers. Moran's I, which is used in this study, is a statistic specially designed for testing the significance of spatial autocorrelation. Once found to be spatially correlated, the data are sampled in a way that ensures their efficient use and limits the effect of correlations. To develop the sampling strategy and to test for spatial autocorrelation of the sampled data requires knowledge of the spatial autocorrelation of reflectance in the unsampled data. The spatial autocorrelation coefficient was therefore computed along and across the satellite track using the data from 1, 10, 19, and 29 July 1985 in the region north of 60°N. The autocorrelation coefficient gradually decreases from unity toward zero with a scale length of about 500 km, indicating that two reflectance measurements must have a large separation to be completely independent. No significant difference is found between the autocorrelation coefficients calculated along and across the satellite track when the autocorrelation is expressed in terms of distance. However, since pixel size varies with viewing zenith angle and the radiometers scan across the track, the autocorrelation coefficient expressed as a function of pixel number differs in the along- and across-track directions and also depends on the position of the initial pixel. These features of the autocorrelation are considered in the design of a sampling scheme to eliminate spatial dependence.

In addition to sampling, the original data are subject to narrowband and broadband pixel matching, scene selection, and homogeneity screening conditions in order to produce spatially independent, homogeneous, and spatially and temporally matched ocean, land, ice–snow, and cloud datasets. Broadband reflectance is

found to differ markedly from the narrowband reflectances in both shortwave channels of the AVHRR, but it is fairly linearly correlated, which allows prediction of broadband reflectance from narrowband measurements. Five linear regression functions of R_1 and R_2 are developed using the data from 1, 10, and 29 July 1985. The data from 19 July serve as independent data to test models. The models for ice/snow and clouds are found to be able to estimate broadband reflectance very accurately, the explained variance being 97% and 93%, respectively. The models for ocean and land produce larger uncertainties. In comparison with previous models, improvements are achieved in terms of both accuracy and reliability of the regression analysis, owing to the better data matchups and the attention paid to the selection of uncorrelated data.

In addition, the influence on the regression models of scene identification, inclusion of the channel 2 reflectance, and geometric parameters are investigated. The two-channel scene-independent model provides virtually as good predictions for undifferentiated scenes as do the scene-specific models for their corresponding scene type. However, systematic errors are generated if the scene-independent models are applied to homogeneous scenes. The use of channel 2 reflectance significantly improves the determination of broadband reflectance by the scene-independent model, produces a small improvement in the model for land, but has little impact on the other scene-specific models. Finally, no significant effect is found on the regressions of either viewing zenith angle or solar zenith angle.

Acknowledgments. The authors are grateful to two anonymous reviewers for their valuable suggestions to improve the original manuscript. The authors also wish to express their thanks to Prof. Roger Davies for providing the ERBE data and for his helpful comments. Discussions with Dr. Jian Sheng are gratefully acknowledged. The assistance of Ursula Seidenfuss with the diagrams is very much appreciated. This work was supported partially by the grants from the Canadian Atmospheric Environment Service and the Natural Sciences and Engineering Research Council.

REFERENCES

Cess, R. D., and G. L. Potter, 1986: Narrow- and broadband satellite measurements of shortwave radiation: Conversion simulations with a general circulation model. *J. Climate Appl. Meteor.*, **25**, 1977–1984.

——, and I. L. Vulis, 1989: Inferring surface solar absorption from broadband satellite measurements. *J. Climate*, **2**, 974–985.

Cliff, A. D., and J. K. Ord, 1973: *Spatial Autocorrelation.* Pion, 178 pp.

——, and ——, 1981: *Spatial Processes: Models and Applications.* Pion, 266 pp.

Chatterjee, S., 1977: *Regression Analysis by Example.* Wiley, 228 pp.

Davis, P. A., E. R. Major, and H. Jacobowitz, 1984: An assessment of *NIMBUS-7* ERB shortwave scanner data by correlative analysis with narrowband CZCS data. *J. Geophys. Res.*, **89**, 5077–5088.

Dedieu, G., P. Y. Deschamps, and Y. H. Kerr, 1987: Satellite estimation of solar irradiance at the surface of the earth and of surface albedo using a physical model applied to Meteosat data. *J. Climate Appl. Meteor.*, **26**, 79–87.

Ellingson, R. G., D. J. Yanuk, Hai-Tien Lee, and A. Gruber, 1989: A technique for estimating outgoing longwave radiation from HIRS radiance observations. *J. Atmos. Oceanic Technol.*, **6**, 706–711.

Gautier, C., G. Diak, and S. Masse, 1980: A simple physical model to estimate incident solar radiation at the surface from GOES satellite data. *J. Appl. Meteor.*, **19**, 1005–1012.

Gruber, A., I. Ruff, and C. Earnest, 1983: Determination of the planetary radiation budget from *TIROS-N* satellites. NOAA Tech. Rep., NESDIS 3, 12 pp.

Li, Z., and H. Leighton, 1991: Scene identification and its effect on cloud radiative forcing in the Arctic. *J. Geophy. Res.*, **96**, 9175–9188.

Minnis, P., and E. F. Harrison, 1984: Diurnal variability of regional cloud and clear-sky radiative parameters derived from GOES data. Part III: November 1978 radiative parameters. *J. Climate Appl. Meteor.*, **23**, 1032–1050.

Miron, J., 1984: Spatial autocorrelation in regression analysis: A beginner's guide. *Spatial Statistics and Models*, G. L. Gaile and C. J. Willmott, Eds., Reidel, 201–222.

Nunez, M., T. L. Hart, and J. D. Kalma, 1984: Estimating solar radiation in a tropical environment using satellite data. *J. Climatol.*, **4**, 573–585.

Odland, J., 1988: *Spatial Autocorrelation.* Sage, 85 pp.

Ohring, G., and A. Gruber, 1983: Satellite radiation observations and climate theory. *Adv. Geophy.*, **24**, 237–304.

Payette, F., 1989: Application of a sampling strategy for the ERBE scanner data. *CRG Rep.* No. 89-1, McGill University, 100 pp.

Pinker, R. T., and J. A. Ewing, 1986: Effect of surface properties on the narrow to broadband spectral relationship in satellite observations. *Remote Sens. Envir.*, **20**, 267–282.

——, and ——, 1987: Simulations of the GOES visible sensor to changing surface and atmospheric conditions. *J. Geophy. Res.*, **92**, 4001–4009.

Sakellariou, N., and H. G. Leighton, 1988: Identification of cloud-free pixels in inhomogeneous surfaces from AVHRR radiances. *J. Geophy. Res.*, **93**, 5287–5293.

——, ——, and Z. Li, 1992: Identification of clear and cloudy pixels at high latitudes from AVHRR radiances. *Int. J. Remote Sens.*, (accepted).

Staylor, W. F., 1985: Reflection and emission models for clouds derived from Nimbus 7 ERB scanner measurements. *J. Geophys. Res.*, **90**, 8075–8079.

——, and J. Suttles, 1986: Reflection and emission models for deserts derived from *Nimbus-7* ERB scanner measurements. *J. Climate Appl. Meteor.*, **25**, 196–202.

Stowe, L. L., 1988: Report of the earth radiation budget requirements review–1987. NOAA Tech. Rep., NESDIS 41, 103 pp.

Stum, J., B. Pinty and D. Ramond, 1985: A parameterization of broadband conversion factors for METEOSAT visible radiances. *J. Climate Appl. Meteor.*, **24**, 1377–1382.

Vulis, I. L., and R. D. Cess, 1989: Interpretation of surface and planetary directional albedos for vegetated regions. *J. Climate*, **2**, 986–996.

Wydick, J. E., P. A. Davis, and A. Gruber, 1987: Estimation of broadband planetary albedo from operational narrowband satellite measurements. NOAA Tech. Rep., NESDIS 27, 32 pp.